

Specifying an MOAO-fed integral field spectrograph for the E-ELT

M. Puech^{a,b}, P. Rosati^a, S. Toft^a, B. Neichel^{b,c}, and T. Fusco^c

^aEuropean Southern Observatory, Karl-Schwarzschild-Strasse 2, 85748 Garching bei München, Germany

^bGEPI, Observatoire de Paris, CNRS, University Paris Diderot, 5 Place Jules Janssen, 92190 Meudon, France

^cONERA, BP 72, 92322 Chatillon Cedex, France

ABSTRACT

We present an end-to-end simulator for 3D spectroscopy, which can be used to specify MOAO-fed integral field spectrographs dedicated to ELTs. This simulator re-scales either local data or outputs of hydro-dynamical simulations to model distant galaxies. We present simulations of 3D observations in the H-band, for a rotating disk and a major merger at $z=4$, and a large range of stellar-mass. We use these simulations to explore the parameter space, focusing on the impact of the telescope diameter, total integration time, spectral resolution, and IFU pixel scale. The size of the telescope diameter has little influence on the spatial resolution of 3D observations but largely influences the achieved SNR. The choice of the IFU pixel scale is driven by the optimal “scale-coupling”, i.e., the relation between the spatial resolution of 3D observations and the physical size of the features for which one needs to recover the kinematics using this IFU, and the SNR achieved with this spatial scale. To recover the dynamical state of distant emission line galaxies, one of the main goal of such future instruments, one only needs to recover their large-scale motions, which in turn requires only relatively coarse IFU pixel scales (50-75 mas) and moderate spectral resolution ($R=5000$).

Keywords: 3D spectroscopy, Integral Field Spectroscopy, Multi-Object Adaptive Optics, Simulations.

1. INTRODUCTION

Developing a coherent model for the mass assembly of galaxies over cosmic time is a complex and difficult task, which will require a multi-object integral field spectrograph on an ELT¹. Because of the intrinsic small size of distant galaxies, Adaptive Optics (AO) will be needed to keep the spectroscopic signal-to-noise ratio (SNR) high enough to be able to spatially resolve their spectra. However, correcting a large field of view ($\text{FoV} \gtrsim 5$ arcmin) as required to observe many galaxies simultaneously is challenging and normal single natural guide star AO, or even most sophisticated MCAO techniques cannot provide good enough corrections over so large FoVs. MOAO (Multi-Object Adaptive Optics) has been proposed to precisely reach such a goal. The basis of this concept is to correct only regions where the targets lie, instead of correcting the entire FoV of the instrument. The concept of MOAO was first proposed in the FALCON design study, a multi objects 3D spectrograph intended for the VLT^{2,3}. The general concept of MOAO was subsequently adapted to the future European Extremely Large Telescope (E-ELT) in the WFSPEC study⁴, which was a precursor to the current EAGLE concept⁵. Such instruments will be decisive in our capability to further understand the galaxy mass assembly processes as a function of time, and it is thus important to investigate the relation between their characteristics and their scientific capabilities.

One of the main goal of MOAO-fed 3D spectrographs will be to understand the physics of distant emission line galaxies. Resolved kinematics of such galaxies provides a useful testbed for MOAO-fed spectrograph, because it drives the stringent requirements on the Signal-to-Noise Ratio (SNR): while flux is the zero-order moment of an emission line, the velocity and velocity dispersion are derived from the position and the width of emission lines, which are their first and second moments, and higher order moments always have more relative measurement uncertainty. Because of the complex interplay between spatial and spectral features and our limited knowledge of high redshift galaxies, it is helpful, perhaps necessary, to rely on numerical simulations for constraining the design parameters of this new kind of MOAO-fed instruments. For this purpose, we have developed software that simulate end-to-end the emission line characteristics of local galaxies and how they would appear in the distant Universe. By exploring the instrument parameter space (e.g., resolution, pixel scale, or point spread function), it is possible to constrain the instrumental characteristics and performance against a set of galaxy characteristics (e.g., velocity field).

We used such a software to produce first simulations and explore performances using a few scientifically-motivated cases⁶. They illustrated the concept of “scale-coupling”, i.e., the relationship between the IFU pixel scale and the size of the kinematic features that need to be recovered by 3D spectroscopy in order to understand the nature of the galaxy and its substructure. Largest spatial scales are of particular interest because they carry most of the kinematic information useful to reveal the process underlying galaxy dynamics^{7,8}, i.e., whether a given galaxy is in a coherent and stable dynamical state (e.g., rotation), or, on the contrary, out of equilibrium (e.g., subsequently to a merger). In this case, one just needs to recover enough kinematic information on large spatial scales to allow distinguishing between a rotating disk and a major merger, which requires only relatively coarse spatial resolution and modest spatial-mean SNR (typically 5). From this point of view, on a 42m telescope, the choice of an IFU pixel scale of 50-75 mas seems to be sufficient: such a coarse sampling has the benefit of lowering the exposure time to reach this specific SNR (i.e., typically within one night of exposure time) as well as relaxing the performance of the MOAO system (i.e., relatively moderate Ensquared Energy [EE] at a given spatial scale, i.e., the fraction of light under the PSF that enters a given aperture). On the other hand, if one wants to recover the full 2D kinematics of these galaxies (i.e., including features like faint surface brightness regions such as tidal tails produced during mergers), then relatively good MOAO corrections are required: recovering the full 2D-kinematics in $z=4$ galaxies requires relatively long integration times (typically 24 hours on-source) with at least an EE of 34% in 150 mas, i.e., 2 pixels of 75 mas. This EE provides a good “PSF contrast”, which characterizes the amount of light polluting adjacent spectra⁶.

Here, we present the latest version of the simulation pipeline. In the frame of the ESO E-ELT Design Reference Mission, we have undertaken a much wider exploration of the parameter space. As a very minimal goal for such instruments, we require the 3D detection of distant galaxies with a spatial-mean SNR of 5, which should provide enough information to recover their dynamical state through their large-scale motions⁶. Here, we focus on which range of the instrument parameter space (e.g., spectral resolution, pixel scale) allows us to reach such a SNR.

2. AN END-TO-END SIMULATION PIPELINE FOR 3D SPECTROSCOPY

2.1 General Description

The main steps of the process can be summarized as follows. First, a data-cube with the spatial resolution of the telescope diffraction limit (i.e., $\sim\lambda/2D$, where D is the telescope diameter) is generated. In each pixel of this high resolution data-cube, a spectrum is constructed from observations of local galaxies or numerical simulations. The second step consists in reducing the spatial resolution of the data-cube by convolving each spectral channel of the high resolution data-cube by a PSF. This PSF used in this convolution is representative of the optical path through the

atmosphere and the telescope up to the output of the (optional) AO system. In the third step, the spatial sampling of the data-cube is reduced to match that of the IFU of the simulated instrument. Finally, realistic sky and thermal backgrounds, as well as photon and detector noise are added. We now describe each step in details.

2.2 High resolution data-cube

At very high spatial resolution, emission lines with kinematics driven only by gravitational motions are well described by a simple Gaussian⁹. Under this assumption, within each pixel of the data-cube, only four parameters are needed to fully define a spectral line. The first three parameters are the position in wavelength, the width, and the area (or, equivalently the height) of the emission line. The current version of the software only models emission lines and does not take into account the detailed shape of the continuum in galaxies - it is simply modeled as a constant in f_λ . So only one parameter is required to set the level of this pseudo-continuum around the emission line. Each spectrum is generated in the observational frame, at a given spectral sampling of $\lambda/2R$, where R is the spectroscopic power of resolution of the instrument, and $\lambda_{\text{obs}}=(1+z)\cdot\lambda_{\text{em}}$, λ_{em} being the rest-frame wavelength of the emission line, and z the redshift of the simulated object. During this process, the rest-frame line width is multiplied by $(1+z)$, as one needs to take into account the widening of emission lines with increasing redshift.

All these four parameters can be extracted from observations of local galaxies. In the following, we use Fabry-Perot (FP) observations of the H α emission distributions of nearby galaxies obtained as part of the GHASP survey¹⁰. From these data, we can extract four parameters, wavelength, width, area, and continuum level to construct the velocity field, the velocity dispersion map, the flux map of the H α emitting gas, and the continuum map of the galaxy. The software first re-scales all these maps at a given angular size (in arcsec) provided by the user. These maps are then interpolated at a spatial sampling of $\lambda/2D$. This spatial sampling is motivated by the fact that the AO PSFs used is the following have been simulated at this sampling (see Sect. 2.4). The software then re-scales the overall amplitude of the continuum map at a given integrated number of photons using an integrated magnitude m_{AB} directly provided by the user. This magnitude is converted to the number of photons per spectral pixel depending on the telescope diameter D , the integration time t_{intg} , and the global transmission t_{trans} of the system (atmosphere excluded). The overall amplitude of the H α map is also rescaled at a given integrated number of photons, derived from the integrated continuum value and a rest-frame equivalent width EW_0 provided by the user, the latter being re-scaled in the observed-frame by multiplying by $(1+z)$. All parameters can also be extracted from outputs of hydro-dynamical simulations¹¹. In this case, the two last parameters (area and continuum level) can respectively be extracted from total gas and stellar surface density maps which are by-products of the numerical simulation, also rescaled in terms of size and flux.

2.3 Modeling the IFU and the detector

Each monochromatic slice of the high resolution data-cube is convolved by a PSF with matching spatial sampling. This PSF must be representative of all elements along the optical path, from the atmosphere to the output of an (optional) Adaptive Optic system. Because the isoplanetic patch¹² (the median value at Paranal is ~ 2.4 arcsec at $\lambda \sim 0.5 \mu\text{m}$, which leads, e.g., to ~ 10 arcsec at $\lambda \sim 1.6 \mu\text{m}$) is larger than the individual FoV of the IFU (typically a few arcsec, depending on the size of objects at a given redshift), the same PSF can be used to convolve the data-cube regardless of position within the IFU. We also neglected the variation of the PSF with wavelength (with a FWHM scaling as $\lambda^{-1/5}$ in a Kolmogorov model of the atmospheric turbulence¹³), as we are only interested in the narrow spectral range around a single emission line.

The next step consists in reducing the spatial sampling of the data-cube. This is done by re-binning each monochromatic

channel of the data-cube at the pixel size Δ_{pix} of the simulated IFU. A wavelength dependent atmospheric absorption curve taken from ESO Paranal¹ is then applied to each spectrum of the data-cube. Sky continuum, detector dark level, bias, and thermal background are then added to the spectra. We used a sky spectrum model (including zodiacal emission, thermal emission from the atmosphere, and an average amount of moonlight) from Mauna Kea², which has the advantage over other available sky spectra to be very well sampled with $0.2 \text{ \AA}/\text{pixel}$. Thermal backgrounds are modeled using grey bodies parametrized by a temperature T and an emissivity ϵ , i.e., a black body of temperature T multiplied by a constant emissivity ϵ . Photon and detector noise are then added. The detector noise is due to the dark current (dark), readout noise (ron), and the Charge Transfer Efficiency (CTE), which is important for optical arrays. CTE is modeled as $\sigma_{\text{CTE}} = \sqrt{2 \cdot (1 - \text{CTE}^p) \cdot N_{\text{photons}}}$, where N_{photons} is the number of photons in a given spectral pixel, and p is one fourth of the detector size (in pixels).

Finally, the simulation pipeline generates n_{dit} data-cubes with individual exposure time of dit , which are combined by estimating the median of each pixel to simulate several individual realistic exposures. Since we have only included random noise, it is similar to having dithered all of individual exposures and combining after aligning them spatially and spectrally. Sky frames are evaluated separately (i.e., with a different noise realization), and then subtracted to each individual “science” frame.

2.4 Modeling MOAO PSFs

The coupling between the MOAO system and the 3D spectrograph is captured through the MOAO system PSF. Therefore, it is a crucial element that needs to be carefully simulated, and cannot be approximated by, e.g., a simple Gaussian. In the following, we use a new and full analytical code to generate MOAO PSFs, which has the advantage of producing PSFs without speckle noise, i.e., more representative of long-exposure PSFs¹⁴. Briefly, three off axis guide stars, located at the edges of an equilateral triangle, are used to perform a tomographic measurement of the turbulent atmospheric volume. We have used a turbulent profile typical of that on Cerro Paranal, composed of 10 layers³. The seeing and the outer scale of the turbulence were respectively set to 0.8 arcsec (at 0.5 \mu m) and to 25m (the median values on Paranal). The optimal correction is deduced from the characteristics of the turbulence volume and applied assuming a single Deformable Mirror (DM) per direction of interest, here taken as the center of the guide star constellation. The DM inter-actuator pitch was assumed to be 0.8 m, which roughly corresponds to 53×53 actuators for a 42 m telescope. To explore a wide range of correction, we consider different GS-constellation sizes, from 4 to 0.25 arcmin in diameter. In the H-band, these PSFs provide an Ensquared Energy roughly ranging from 20 to 55 % in an 100 mas square aperture, or, equivalently, a Strehl Ratio ranging from 1 to 36%. Because the EE is directly linked to the achieved SNR⁶, we chose this quantity to characterize MOAO PSFs.

2.5 Outputs

The simulated data-cubes are analyzed using an automatic data analysis pipeline similar to those generally used to analyze data of high redshift galaxies. During this process, each spatial pixel of the simulated data-cube is fitted with a Gaussian in wavelength, which position and width correspond to the velocity and velocity dispersion of the gas in this spatial pixel⁶. For each simulated datacube, this analysis pipeline produces a velocity field, a velocity dispersion map, and an emission line flux distribution map. In addition, the simulation pipeline derives a spectroscopic SNR as follows:

¹www.eso.org/observing/etc

²www.gemini.edu/sciops/ObsProcess.obsConstraints/ocSkyBackground.html

³ See details here: http://www.eso.org/sci/facilities/eelt/science/drm/tech_data/ao/

$$SNR(i_x, j_y, k_\lambda) = \frac{O(i_x, j_y, k_\lambda) * \sqrt{ndit}}{\sqrt{O(i_x, j_y, k_\lambda) + S(i_x, j_y, k_\lambda) + ron^2 + dark}},$$

where $O(i_x, j_y, k_\lambda)$ and $S(i_x, j_y, k_\lambda)$ are respectively the object and sky flux per dit (after accounting for atmospheric transmission) in the spatial position (i_x, j_y) of the data-cube (in pixels), and at the spectral position k_λ along the wavelength axis (in pixels). The analysis pipeline uses this information to construct a SNR map, which gives $MAX_{k_\lambda}[SNR(i_x, j_y, k_\lambda)]$, i.e., a map of the maximal SNR in the emission line. From this map, a mean SNR is derived by taking the mean value over the galaxy.

3. SIMULATIONS

3.1 Methodology

All input parameters can be separated into two broad categories, namely the “physical” parameter space, which includes all parameters defining the distant galaxy (i.e., redshift z , diameter S , continuum ABmagnitude m_{AB} , rest-frame emission line equivalent width EW_0 , Morpho-kinematical type), and the “technical” parameter space, which encompasses all parameters defining the telescope (e.g., M1 and M2 sizes), the instrument (e.g., spectral resolution R , IFU pixel size Δ_{pix} , total integration time T_{intg} , temperatures and emissivities, EE, transmission t_{transm}), and the site (e.g., seeing, sky brightness). Given the very large number of parameters to be investigated, as well as the very large range of values to be explored, it is useful to define a “reference case”, around which the parameter space can be explored. As such a reference case, we took an M* galaxy at $z=4$ (see below). At this redshift, the [OII] emission line can be observed in the H-band, where the influence of the thermal background is minimized in comparison with the K-band. This makes this reference case as independent as possible of the telescope design (e.g., number of mirrors), environmental conditions (site selection), and instrument characteristics (e.g., number of warm mirrors), which are not fully known at this point. For simplicity, we assumed that the [OII] emission line is a single line, instead of a doublet. This does not influence any results presented here, which all scale with the *total* flux, i.e. the flux inside both lines of the doublet.

Our goal is to investigate variations in the technical parameter space that allows to reach a minimal SNR of 5. We chose to explore variations in the $\{T_{intg}, M1, M2, R, \Delta_{pix}, t_{transm}\}$ parameter sub-space, i.e., those driving the number of photons reaching the detector for a given physical parameter space. Variations in EE were explored elsewhere⁶, and here we use the 0.5-arcmin MOAO configuration as described in Sect. 2.4, which provides an EE of 46% (in 100 mas), or a Strehl Ratio of 28%. This configuration provides a relatively good correction, representative of good MOAO corrections. For simplicity, we assumed no central aperture ($M2=0$), so that in the following, the telescope effective aperture is simply equal to the M1 diameter D . Moreover, the number of photons reaching the detector is a degenerated function of some parameters, e.g., the same number of photons can be obtained by varying the global transmission t_{transm} at constant T_{intg} or varying T_{intg} at constant transmission t_{transm} , with no influence on the spatial or spectral resolution. Hence, we chose to further reduce the investigated sub-space of parameters to $\{T_{intg}, D, R, \Delta_{pix}\}$, which will be referred to as the “instrument” parameter space in the following. We nos detail how other parameters were set up.

3.2 Technical parameters

- Telescope diameter D : we chose to follow the E-ELT baseline, which has a 42m primary mirror M1. We also explored $D=30m$, as in the Thirty Meter Telescope project;

- Global transmission (excluding the atmosphere): for the E-ELT, the global throughput is estimated to range between 80 and 92%, depending on coating⁴; for the IR detector, a reasonable value is 90%; for the instrument, we assumed a throughput of 30%, which is representative of current NIR 3D spectrographs. Therefore, we assumed a conservative global transmission of 20%;
- IFU pixel scale Δ_{pix} : we assumed a pixel scale of 50 mas for the reference case⁶. We also explored pixel scales of 25 and 75 mas;
- Spectral resolution R: we assumed a spectral power of resolution R=5000 for the reference case. We also explored R=2500 and R=10000;
- NIR detector characteristics: as a point, with IR arrays, there is no CTE since charge is not transferred in these devices. For the dark current and read-out noise, we relied on a cooled Rockwell HAWAII-2RG IR array working at ~80K, with a dark current of 0.01 e⁻/s/pix, and a read-out noise of 2.3 e⁻/pix¹⁵. For simplicity, we assumed no saturation threshold for the NIR detector;
- Exposure time T_{intg} : we assumed a reference case exposure time of 24 hours⁶. Because observations of distant galaxies in the NIR are generally not limited by the detector noise, we did not explore variations of the individual frame exposure time dit and chose dit=3600 seconds and ndit=24. We also explored ndit=8, which corresponds to a total exposure time of 8 hours;
- Telescope temperature and emissivity: we adopted a temperature of 280 K and an emissivity of 5%. The latter depends on the mirror coating, and we assumed a relatively optimistic value, as the emissivity of the 5-mirror design E-ELT could be as large as ~ 15%⁴;
- Instrument temperature and emissivity: we followed a preliminary study of the thermal emissivity of EAGLE, the project of multi-objects integral field spectrograph for the E-ELT¹⁶. The target acquisition system was assumed to have a temperature of 240 K and an emissivity of 15 %, while the spectrograph was assumed to have a temperature of 150 K and an emissivity of 69 %. The detector was assumed to be cooled at 80 K, and its thermal background was therefore neglected.

3.3 Scientific inputs

A full description will be given in a forthcoming paper (Puech et al., in prep.). However, for sake of completeness, we give here a brief description of how they were derived (see also Table 1):

- Galaxy continuum magnitude m_{AB} : we used empirical relations, derived from the MUSIC sample¹⁷, between M^* which characterizes the knee of the stellar-mass function at this redshift⁵) and K-band magnitude K_{AB} to estimate a realistic continuum flux for a given stellar mass and redshift. We directly used this value to define the pseudo-continuum level around the [OII] emission line, and did not apply any “color” correction between the observed wavelength of the emission line (~1.86 μm) and that of the H or K-band (~1.65 or 2.2 μm). Such an assumption is consistent with Spectral Energy Distributions of galaxies with a morphological type later than Sa within a factor two in flux. For the reference case, we assumed an M^* galaxy at $z=4$. We also explored fainter and brighter galaxies at the same redshift, corresponding to 0.1 M^* , 0.5 M^* , 5 M^* , and 10 M^* (see Table 1);
- Galaxy size S: the galaxy diameter was assumed to be four times the average median UV half-light radius at $z=4$ ^{18,19,20}. The UV half-light radius was converted into an half-light radius at $\lambda=3727 \text{ \AA}$ ²¹ and rescaled for a given stellar-mass M_{stellar} using a local scaling relation with the K-band luminosity²², i.e., $R_{1/2} \sim L_K^{0.35}$, and assuming that $M_{\text{stellar}} \sim L_K$;

4 http://www.eso.org/sci/facilities/eelt/science/drm/tech_data/telescope/

5 M^* can be seen as the stellar-mass equivalent of L^* , which alternatively characterizes the knee of the luminosity function using a Schechter relation.

- Rotation velocity V_{rot} : we used the local Tully-Fisher relation assuming no evolution⁷. This value was used to roughly rescale the amplitude of the Velocity Field as a function of stellar-mass;
- Rest-frame emission line equivalent width EW_0 : we assumed $EW_0([\text{OII}])=30 \text{ \AA}$, which is an extrapolation of the median value found at $z\sim 1$ ²³. This parameter does not influence the flux distribution of the galaxy but is used to set its total integrated value (see Section 2). It therefore produces an additional degeneracy on the number of photons reaching the detector, as the one described above between transmission and total integration time. For this reason, we also explored a lower value of $EW_0([\text{OII}])=15 \text{ \AA}$, and abusively included EW_0 in the “instrument” parameter space;
- Morpho-kinematical template: to see how the mean SNR is influenced by the 2D morphological and kinematical distributions, we used two templates representative of the two extreme large-scale variations encountered in the morpho-kinematics of emission line galaxies⁶ (see Fig. 1). The first one is a local Sab rotating spiral disk, which was selected from the GHASP survey¹⁰. The second one is an hydrodynamical simulation of a major merger between two Sbc galaxies¹¹.

M^*/M_{\odot}	$\text{Log}(M_{\text{stellar}}/M_{\odot})$	K_{AB} (mag)	V_{rot} (km/s)	Diameter (")
0.1	9.7	26.8	130	0.33
0.5	10.4	25.1	180	0.59
1.0	10.7	24.3	200	0.75
5.0	11.4	22.6	300	1.30
10.0	11.7	21.8	330	1.70

Table 1: Scientific inputs for simulations of $z=4$ galaxies of different stellar mass. From left to right: fraction of M^* at $z=4$, corresponding stellar-mass in solar units, K-band AB magnitude, rotation velocity, and assumed galaxy diameter, in arcsec.

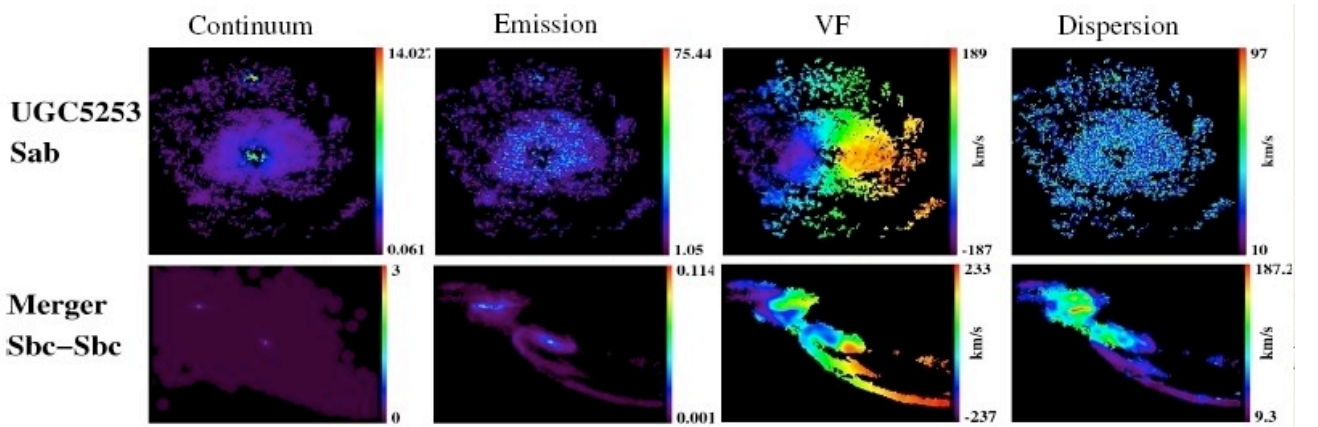


Figure 1: Morpho-kinematical templates used for the simulations. First line: Sab rotating disk from the GHASP survey. Second line: a major merger between two Sbc galaxies from hydrodynamical simulations. From left to right: continuum map, emission line map, velocity field, and velocity dispersion map.

4. RESULTS

4.1 Signal to Noise Ratio

Because we are interested in recovering large-scale motions, it is sufficient to characterize the SNR over the galaxy size, using a simple spatial mean as defined in Sect. 2.5. In the H-band, the achieved spatial-mean SNR is found to be limited by the galaxy flux shot-noise, for all the stellar-mass range and emission line equivalent widths explored in the simulations: the $z=4$ reference case has a mean surface brightness $\sim 2 \text{ mag/arcsec}^2$ brighter than the total background. The thermal and sky backgrounds approximately account for 1/5 and 4/5 of the total background, respectively, with the former being largely dominated by the contribution from the telescope ($>90\%$). In such a shot-noise limited regime, one expects to find the spatial-mean SNR varying linearly with (1) the square root of the integration time, (2) the telescope diameter, (3) the rest-frame emission line equivalent width, (4) the inverse square root of the spectral power of resolution, and (5) the pixel size. Simulations confirm all these scalings, as illustrated in Fig. 2.

Therefore, the required minimal spatial-mean SNR of 5 scales as:

$$\langle S/N \rangle_{min} = 5 \left(\frac{T}{24h} \right)^{0.5} \left(\frac{D}{42m} \right) \left(\frac{EW}{30\text{\AA}} \right) \left(\frac{R}{5000} \right)^{-0.5} \left(\frac{\Delta pix}{50 \text{ mas}} \right)$$

Because MOAO provides only partial seeing corrections, the resulting PSF is dominated by residual atmospheric perturbations: the telescope diameter does not influence the spatial resolution of observations, but only the achieved SNR. The above scaling relations show that there is no breaking point in telescope diameter: with a smaller 30m telescope, one would need two times longer exposures to reach the same SNR. Other parameters can influence the achieved SNR without impacting the spatial or spectral resolution: the emission line equivalent width scales as the square root of the total integration time, which means that a two times lower EW_0 requires four times longer exposure times. This scaling also applies to the total instrument transmission, although it was not explicitly explored in the present simulations (see Sect. 3.1).

4.2 Influence of pixel scale

The choice of the IFU pixel scale drives the spatial resolution of MOAO-fed 3D spectroscopy observations, as in the range of EE provided by MOAO, the PSFs have a FWHM largely smaller than twice the pixel size⁶. Therefore, the choice of the optimal IFU pixel scale is related to the optimal “scale-coupling” between the IFU pixel scale and the spatial scale of the physical feature that one wants to recover using this IFU⁶. It can be quantified by using the ratio between the size of this feature (here, the galaxy diameter, as one wants to recover the large-scale rotation) and the size of the IFU resolution element. 3D observations of $z\sim 0.6$ galaxies with FLAMES/GIRAFFE have demonstrated that a scale-coupling of about 3 is already enough to recover large-scale motions^{7,24}. It corresponds to the minimum value necessary to ensure that each side of the galaxy is at least spatially sampled by the IFU at the Nyquist rate. In the $z\sim 4$ simulations, this minimal scale-coupling leads to a pixel scale of $\sim 55\text{mas}$, 125 mas , and 280 mas for 0.1 , 1 , and $10 M^*$ galaxies, respectively. Hence, a minimal pixel scale of 50 mas is required if one wants to be able to recover, at least in principle, large-scales motions in $z\sim 4$ galaxies, and for a large range of stellar-mass.

In Fig. 3, we show the velocity fields, velocity dispersion maps, and emission line maps extracted from the simulations using a 50 mas pixel scale. One can easily see that the lowest mass case barely provides enough spatial information to clearly distinguish between the rotating disk and the major merger. Even if the scale-coupling is in principle large enough to properly recover large-scale motions, the pixel scale limits the achieved SNR to relatively low values (see Fig. 2). If one only wants to recover large-scale motions in larger mass objects, then an IFU pixel scale of 75 mas can be used⁶, providing more SNR at constant integration time (see Fig. 2).

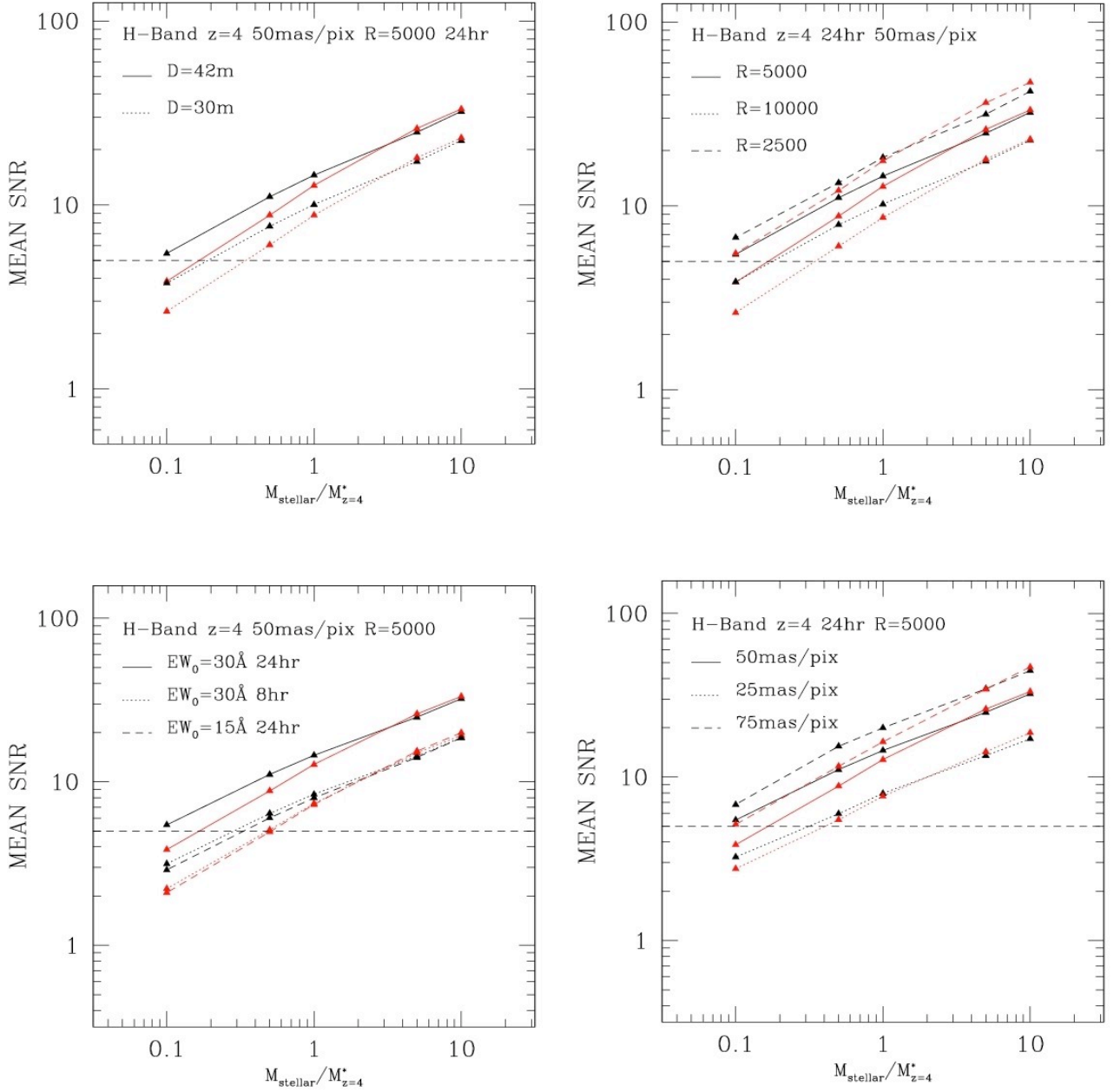


Figure 2: Spatial-mean SNR for an M^* galaxy at $z=4$ depending on instrument parameters. Upper-left panel: influence of telescope diameter. Upper-right panel: influence of spectral resolution. Lower-left panel: influence of integration time and EW_0 . Lower-right panel: influence of pixel size. In all panels, the stellar-mass ranges from 0.1 to $10 M^*$, black lines represent simulations of a rotating disk, red lines represent simulations of a major merger. In all panels, solid lines represent the reference case (see text).

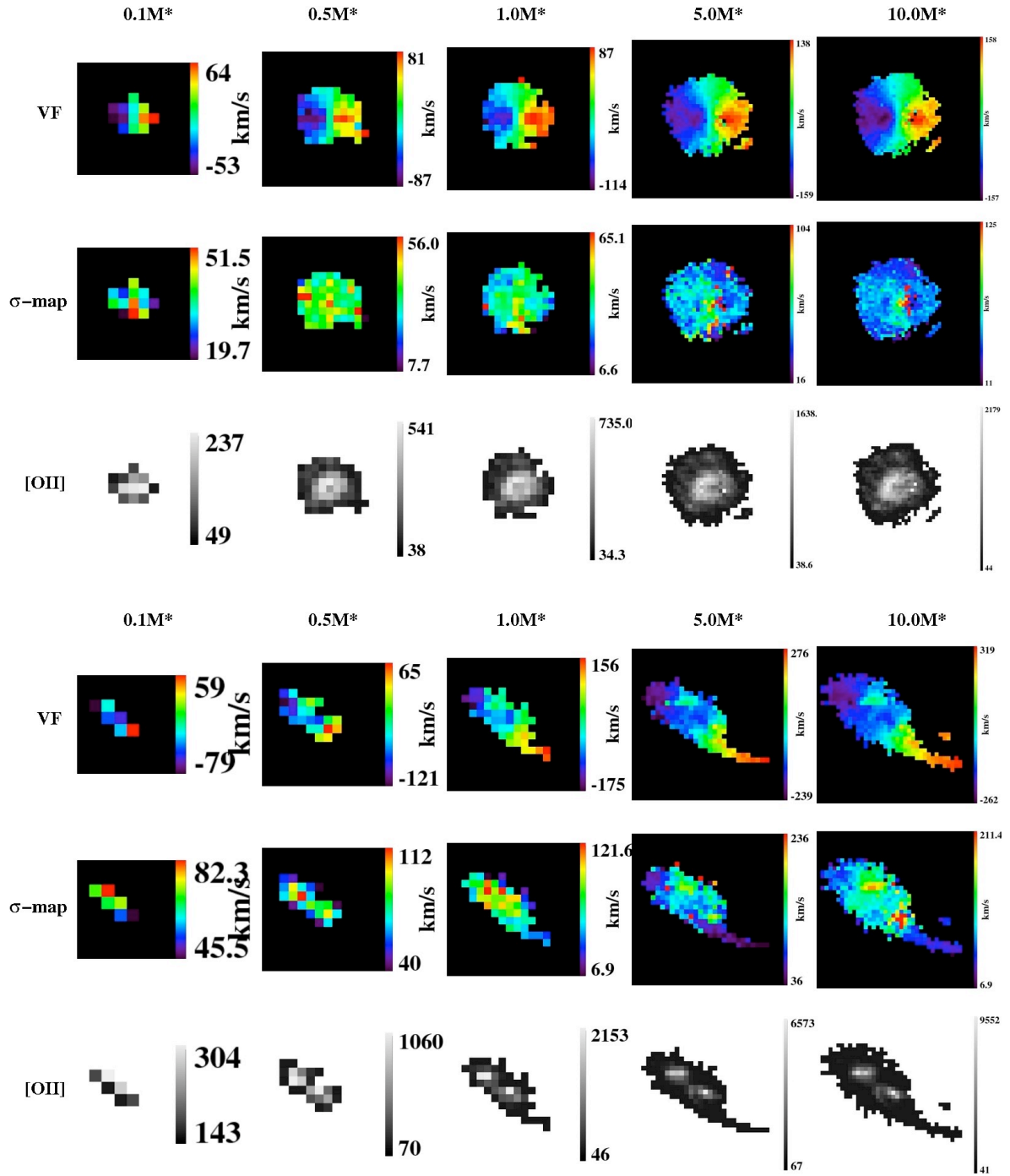


Figure 3: Simulations of $z=4$ galaxies. Each column represent simulations for a different stellar-mass, from 0,1 to 10 M^* . The three upper lines show the velocity fields, velocity dispersion maps, and the emission line maps for a rotating disk, while the three lower lines show the same maps for the major merger case.

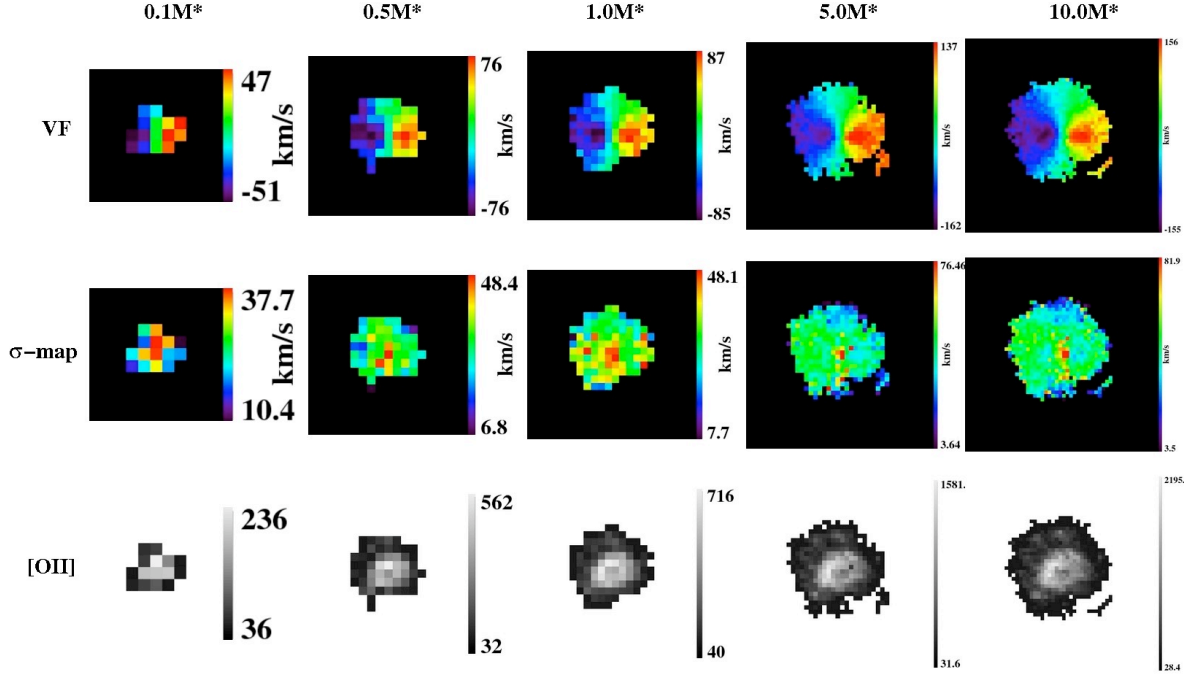


Figure 4: Simulations of a $z=4$ rotating disk, with 50 mas per pixel and $R=10000$. Each column represents simulations for a different stellar-mass, from 0,1 to 10 M^* . From top to bottom: velocity fields, velocity dispersion maps, and emission line maps.

4.3 Influence of spectral resolution

Appropriate targets in the NIR are usually selected such as they have emission lines that fall in regions free of strong OH lines. This requires a minimal spectral resolution of $R \sim 3000$ to resolve OH sky lines with enough accuracy. On the other hand, the higher the spectral resolution, the better the accuracy on the recovered kinematics. In Fig. 4, we show the velocity field, velocity dispersion maps, and emission line maps extracted from the simulations of a rotating disk at $z=4$, using a 50 mas pixel scale and $R=10000$. Compared with Fig. 3, the higher spectral resolution allows to reduce the range of measured velocity dispersion. A better spectral resolution also allows a better recovery of the velocity field. However, if one wants to recover only large-scale motions, only the global shape of the kinematics is relevant, and a spectral resolution $R \sim 5000$ seems accurate enough. This value appears to be a good compromise between our desire to minimize the impact of the OH sky lines and not wanting to over-resolve the line by a large factor. Fig. 2 clearly demonstrates the interest of having the smallest spectral resolution possible, which optimizes the achieved SNR.

5. CONCLUSIONS

We have presented a new simulation pipeline, which allows end-to-end simulations of MOAO-fed 3D spectrographs. Such simulations allow to directly specify the instrument characteristics relatively to scientific products. We have presented realistic simulations of $z \sim 4$ galaxies for a range of stellar-mass, and explored the instrument parameter space. We have confronted the achieved SNR to expected scaling relations with the instrument parameters, which result from a galaxy shot-noise limited regime. One important scaling is the one between the telescope diameter, which varies as the square root of the total integration time at constant SNR, i.e., there is no breaking point in telescope diameter for 3D observations of distant galaxies. The choice of the IFU pixel scale is driven by the optimal “scale-coupling” between the

spatial resolution of 3D observations, which is set up by the IFU pixel scale for MOAO corrections, and the physical size of the features for which one needs to recover the kinematics using this IFU. To recover the dynamical state of distant galaxies, one can use relatively coarse IFU pixel scales (50-75 mas), as one only needs to recover their large-scale motions. The choice of the spectral resolution is a balance between the need to resolve OH sky lines and select galaxies with emission lines falling between these lines, the accuracy of the recovered 2D kinematics, and the achieved SNR. Focusing on large scale motions only, $R=5000$ seems to be a good compromise.

REFERENCES

1. Hook, I. M. (ed.), 2005, "The Science Case for the European Extremely Large Telescope: The next step in mankind's quest for the Universe"
2. Hammer, F., Sayède, F., Gendron, E., et al., 2002, Proc. of the ESO workshop Scientific Drivers for ESO Future VLT/VLTI Instrumentation, 139
3. Assémat, F., Gendron, E. & Hammer, F., 2007, MNRAS, 376, 287
4. Moretto, G., Bacon, R., Cuby, J.-G., et al., 2006, Proc. SPIE Vol. 6269, 76
5. Cuby J.-G., Morris, S., Bryson, I., et al., 2008, this volume, in press
6. Puech, M., Flores, H., Lehnert, M., et al., 2008, MNRAS, submitted
7. Flores, H., Hammer, F., Puech, M., et al., 2006, A&A, 455, 107
8. Puech, M., Hammer, F., Flores, H., et al., 2006, A&A, 455, 119
9. Beauvais, C., & Bothun, G., 1999, ApJS, 125, 99
10. Amram, P., Adami, C., Balkowski, C., et al., 2002, Ap&SS, 281, 393
11. Cox, T.J., Jonsson, P., Primack, J., et al., 2006, MNRAS, 373, 1013
12. Fried, D.L. 1981, JOSA, 72, 52
13. Roddier, F. 1981, Progress in Optics, 19, 281
14. Neichel, B., Fusco, T., Conan, J.-M., et al., Proc. SPIE Vol. 7015, in press
15. Finger, G., Garnett, J., Bezawada, N., et al., 2006, Nuclear Instruments & Methods in Physics Research A, 565, 241
16. Laporte, P., Chemla, F., Puech M., et al., this volume, in press
17. Grazian A., Fontana, A., de Santis, C., et al., 2006, A&A, 449, 951
18. Bouwens, R.J., Illingworth, G.D., Blakeslee, J.P., et al., 2004, ApJ, 611, 1
19. Ferguson, H.C., Dickinson, M., Giavalisco, M. et al., 2004, ApJ, 600, 107
20. Dahlen, T., Mobasher, B., Dickinson, M., et al. 2007, ApJ, 654, 172
21. Barden, M., Rix, H.-W., Somerville, R. S., et al., 2005, ApJ, 635, 959
22. Courteau, S., Dutton, A. A., van den Bosch, F. C., et al., 2007, ApJ, 671, 203
23. Hammer, F., Flores, H., Lilly, S.J., et al., 1997, ApJ, 481, 49
24. Yang, Y., Flores, H., Hammer, F., et al., 2008, A&A, 477, 789